Intelligent Methodology for Sensing, Modeling and Control of Pulsed GTAW: Part I — Bead-on-Plate Welding

Computer vision for sensing, neural networks for modeling, fuzzy logic and neuron self-learning for control of pulsed GTAW are described

BY S. B. CHEN, Y. J. LOU, L. WU AND D. B. ZHAO

ABSTRACT. This study addresses intelligent techniques for fulfilling quality control of head-on-plate welding. A new visual double-sided sensing system capable of imaging the weld pool topside and backside simultaneously in a frame was provided to determine the weld pool geometry parameters. The imaging principle was analyzed with spectrum distribution, in which the weld pool was illuminated by arc light emission to receive a clear image under base current. Double-sided size parameters describing weld pool geometry were defined and determined in real time with the developed image processing algorithm. The influences of welding parameters such as pulse duty ratio and travel speed on weld bead geometry were identified by step response. Based on the analysis, a neural network model of the dynamic process was established for predicting the backside width with the welding parameters and topside size parameters. The simulation results indicated the accuracy of the model, and the characteristics of the welding process were analyzed carefully. Aiming at the bead-on-plate pulsed GTAW process, conventional and intelligent control methods of single input and single output were investigated, and the neuron self-learning PSD control was verified with better performance for practical application through comparisons.

Introduction

As is well known, weld quality control is a complicated problem in arc welding processes. Backside weld width and penetration depth are major factors in the final weld quality for full penetration. The sensing and control of backside width are critical and challenging issues in automated welding, including robotic welding. Although extensive research has been done to find feasible approaches for sensing these parameters using topside sensors, more practical solutions are still strongly needed for different cases.

In principle, backside weld width and penetration depth can be monitored by embedding thermocouples into the weld piece or by acoustic emission sensing (Ref. 1). However, their practical applications are limited because of the contact between the sensors and the workpiece. In the case of full penetration, the backside weld width can be detected by measuring the light intensity from the backside of the workpiece (Refs. 2–4). However, it is difficult or impossible to conveniently locate backside sensors for many configurations, for instance, during the welding of pressure containers. Also, the motion match between the torch and sensor can be difficult if the torch moves. Hence, the sensor should be attached to and move with the torch to conduct the so-called topside sensing of the weld penetration.

KEY WORDS

Bead-on-Plate Welding
Control Algorithms
Computer Vision
Double-Sided Sensing
Fuzzy Logic
Neural Network Model
Pulsed GTAW

Among the many proposed topside sensing techniques, pool oscillation methods have been extensively studied. The pioneering work was done by Richardson (Ref. 5), Hardt (Ref. 6) and their coworkers. Wang, *et al.* (Ref. 7), found that, for full penetration, the width of a stationary weld pool could be determined by the resonance frequency. An interesting discovery was the distinction of weld pool oscillation frequency between the partial joint penetration and full joint penetration. Xiao and Ouden (Refs. 8, 9) found a drop in the oscillation frequency occurs as the penetration state changes from partial to full penetration. Richardson and Yoo (Ref. 10) have also observed this frequency drop. For the measurement of the pool oscillation, both arc voltage and arc light fluctuations have been used.

Ultrasonic testing has become a standard technique for locating cracks, incomplete fusion, porosity and other discontinuities in fusion welds. Hardt and Katz (Ref. 11) utilized reflection ultrasound methods to measure the size of the stationary weld pool. Ultrasonic measurements of the weld pool were extensively studied at the Idaho National Engineering Laboratory (Refs. 12, 13). Different weld geometries were distinguished. Contact transducers were used. When the ultrasound was generated by a pulsed Nd:YAG laser, the contact transducer could be eliminated (Ref. 14).

Modern infrared thermograph equipment provides a feasible means to measure the temperature field of the weld pool. At Auburn University, the infrared sensing of arc welding has been extensively investigated by Chin, *et al.* (Refs. 15, 16). The temperature distribution is measured in GMAW. It was found the depth of joint penetration can be determined using the characteristics of the temperature profiles. Beardsley, *et al.*

S. B. CHEN, previously with the Harbin Institute of Technology, Harbin, P.R. China, is now with Shanghai Jiao Tong University, Shanghai, P.R. China. Y. J. LOU, L. WU and D. B. ZHAO are with the National Key Laboratory of Advanced Welding Production Technology, Harbin Institute of Technology.

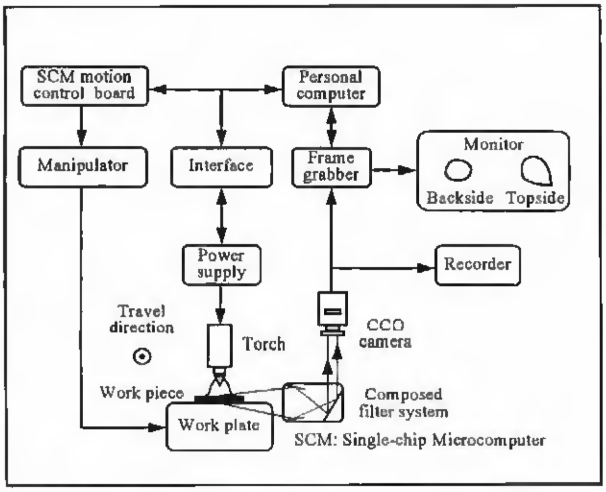

Fig. 1 — Structural diagram of the experimental system.

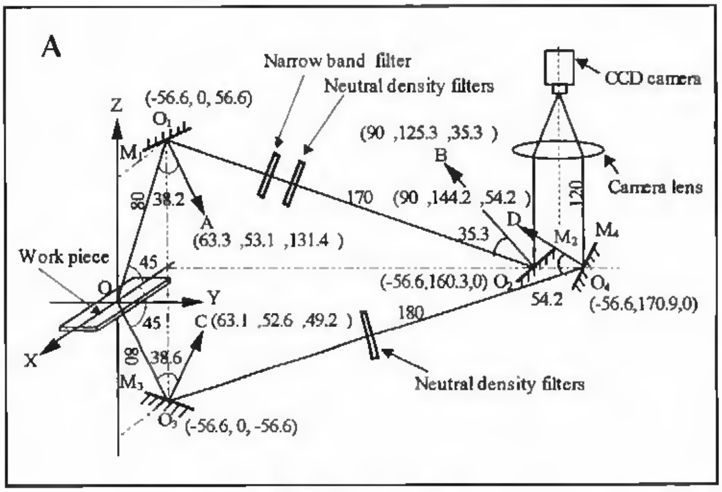

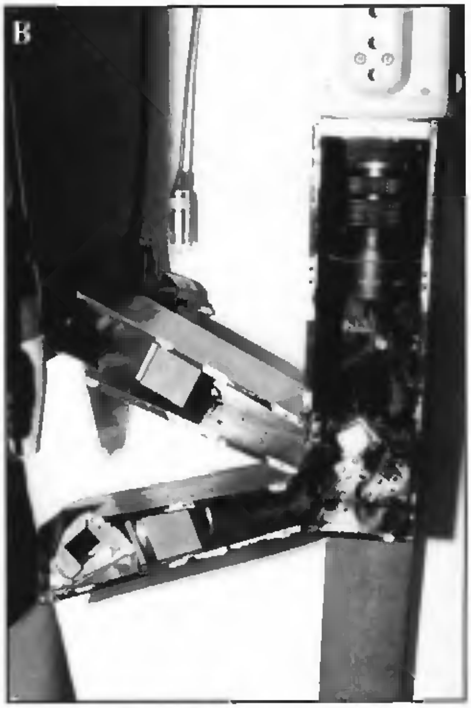

Fig. 2 — The light path of the simultaneous double-sided visual image sensing system of the weld pool in a frame. A — The schematic diagram; B — photograph of sensing system.

(Ref. 17), found the root surface bead width of the full-joint-penetration welds can be determined in GTAW using a ratio between the area of the 600°C isotherm surrounding the weld pool and the weld pool area.

Despite the above achievements in the topside sensing of weld joint penetration, more accurate information can still be determined from the weld pool itself. It is known the weld pool contains abundant information about the welding process. By viewing the weld pool, a skilled operator can estimate the weld joint penetration. Thus, visual sensing systems have been developed to view the weld pool. The visual sensing systems can be divided into two classifications according to the imaging light source: the active method (imaging with another high-intensity light source) and the passive method (imaging with arc light illumination).

The image sensing of the weld pool surface in GTAW has been extensively investigated by Kovacevic, Zhang and coworkers (Refs. 18–20). In their investigation, a high-shutter-speed camera assisted with a pulsed laser was used. The pulse of the laser lasted only 3 ns, and the shutter of the camera was synchronized with the laser pulse. Although the average power of the laser was only 7 mW, its peak power reached 70 kW. During the pulse duration, the intensity of the laser illumination was much stronger than that of the arc and molten metal. Thus, clear images of the weld pool surface could be captured in the GTAW process.

In the passive sensing method, the weld pool images can be illuminated by the arc light emission; therefore, this method has few pieces of hardware, a simple light path of imaging and low application cost. Elementary principle has been carried out to map the visible light emissions in GTAW (Ref. 21). Spectral windows where the external sensors have the least radiance disturbance were proposed and a clear weld pool image was captured. To eliminate the disturbance of unnecessary arc light, Pietrzak (Ref. 22), R. W. Richardson (Ref. 23), D. Brzakovic (Ref. 24) and their coworkers developed a coaxial arc weld pool viewing system, using the electrode tip to block the bright core of the arc from overpowering exposure on the CCD target. Investigations concentrated on a more clear weld pool image, and the intensity of the arc light was found to change from strong to weak when the welding current transformed from pulse peak value to the base value in pulsed GTAW (Ref. 25). The illuminated image of the weld pool was the clearest for determining the weld pool geometry easily.

It should be pointed out the dynamic identification and control of arc welding processes have been explored through a number of studies. The conventional PID control system using current as a control variable was designed (Ref. 26). Advanced control techniques such as adaptive control have also been used to generate sound welds (Refs. 3, 19, 27).

Arc welding is characterized as inherently variable, nonlinear, time varying and having a strong coupling among welding parameters. So, it is very difficult to find a reliable mathematical model and to design an effective control scheme for arc welding by conventional modeling and control methods.

Artificial intelligence methodology was developed for modeling and controling the welding process because it could derive the control performance relying not on the mathematical process model but on human experience, knowledge and logic. Numerous exciting controls with perfect performance have been achieved. K. Andersen (Ref. 28) studied the application for modeling and control of arc welding. T. G. Lim, *et al.* (Ref. 29), proposed an artificial neural network (ANN) model for predicting welding depth, and topside and backside width on-line from the detected surface temperature during GMAW (Ref. 29). During GTAW, the relation between welding current, arc voltage, travel speed, wire feed rate and weld head geometry such as width, depth, reinforcement and cross area was established from an ANN model and trained by experimental data (Ref. 30). Based on weld pool geometrical appearance, Zhang (Refs. 18, 31) developed a control system to simultaneously control the topside and backside pool widths using a neurofuzzy model. A self-learning fuzzy neural network control system of topside width enabled adaptive altering of welding parameters to compensate for changing environments (Refs. 25, 32). Therefore, the control of arc welding seems to be an intelligent and practical application.

In this study, a novel visual sensing system was established to image the topside and backside of the weld pool simultaneously in the same frame. A real-time image processing algorithm was developed to acquire topside and backside sizes of the weld pool. To investigate the dynamic character of arc welding, positive and negative step responses were used to identify the correlation between weld pool geometry and welding parameters. In addition, an artificial neural network model of pulsed GTAW was established. The simulation and analysis of bead-on-plate welds were conducted in pulsed GTAW based on this model. A conventional PID controller, an intelligent fuzzy logic controller and a neuron self-learning PSD controller were designed and compared by simulation results and verified through experiments.

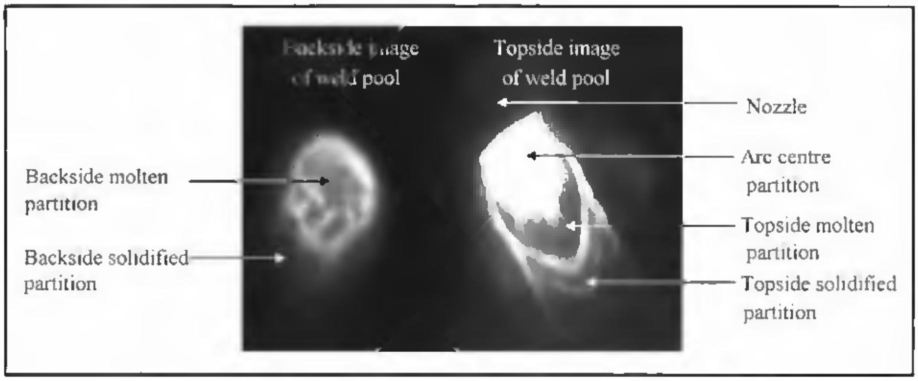

Fig. 3 — A frame of a complete weld pool image of pulsed GTAW.

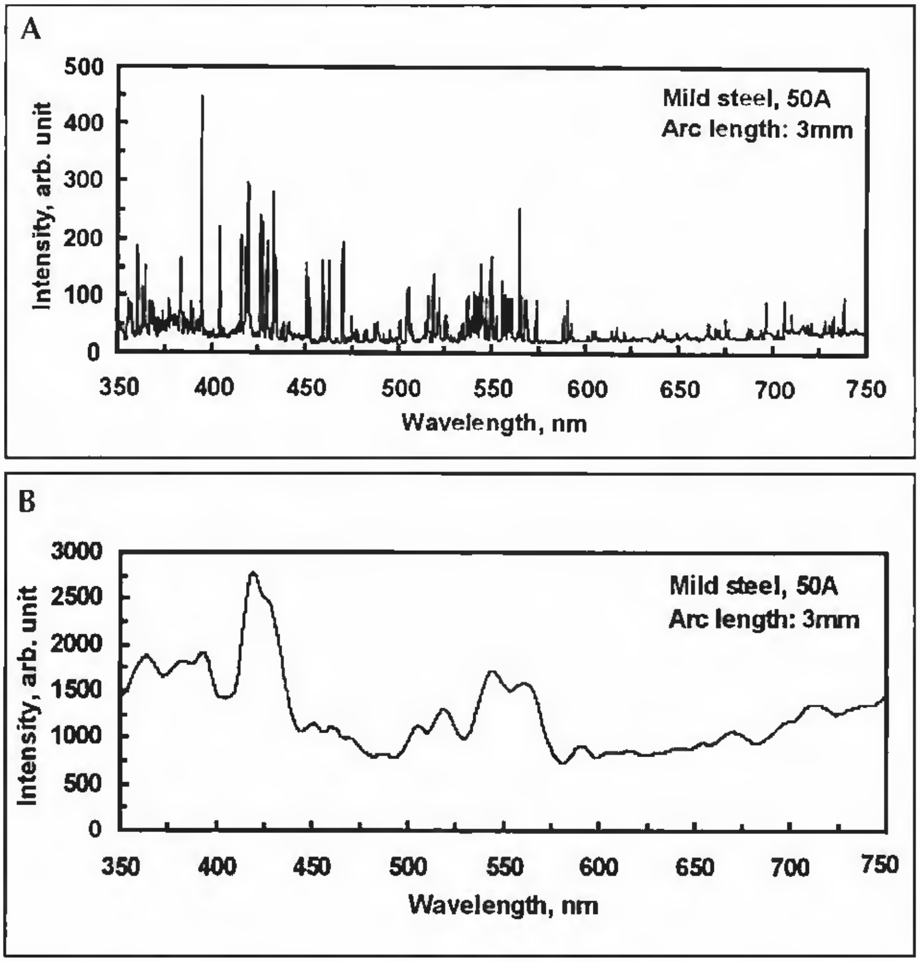

Fig. 4 — Arc light radiation of GTAW with mild steel anode. A — The spectral distribution; B — arc light radiation flux.

Experimental Systems

Experimental Setup

This study addressed the image processing and quality control of pulsed GTAW. The experimental setup included a welding power source, cooling water pump and other auxiliary equipment. The welding current was computer controlled. A diagram of the system is shown in Fig. 1.

Double-Sided Visual Sensing System

Weld joint penetration has a direct influence on weld strength. Although sensors are available to monitor the back of the weld, it is not possible for many applications to access the back face of the weld. Experience of skilled operators suggests the geometry of the weld pool can provide accurate and instantaneous information about the weld penetration. Topside width of the weld pool can be sensed clearly by a CCD camera and a composite filter and controlled accurately (Ref. 25). For further accurate control of weld penetration, the correlation between topside geometry and backside width of the weld pool should be established so that the backside width can be predicted with the determined topside geometry in real time. To correlate the backside width to the topside geometry, both sides of the weld pool need to be imaged simultaneously.

The main parts of the visual sensing system were a composite filter system, CCD camera, recorder, frame grabber and monitor, as shown on the right in Fig. 1. The schematic diagram of the visual sensing system is shown in Fig. 2A, with a photograph in Fig. 2B.

In Fig. 2A, O_XYZ is the workpiece coordinate system and point O is the center point of the weld pool image. M_1, M_2,

Table 1 — Experimental Conditions of Pulsed GTAW

Welding Conditions	Pulse frequency	Pulse duty ratio	Base current	Electrode diameter	Angle of tip	Arc length	Flow rate	Specimen dimension
Unit	f (Hz)	δ (%)	Ib (A)	ϕ (mm)	θ (deg)	1 (mm)	L (L/min)	mm x mm x mm
Value	1	45	60	3.2	30	3.5	8.0	280 x 50 x 2

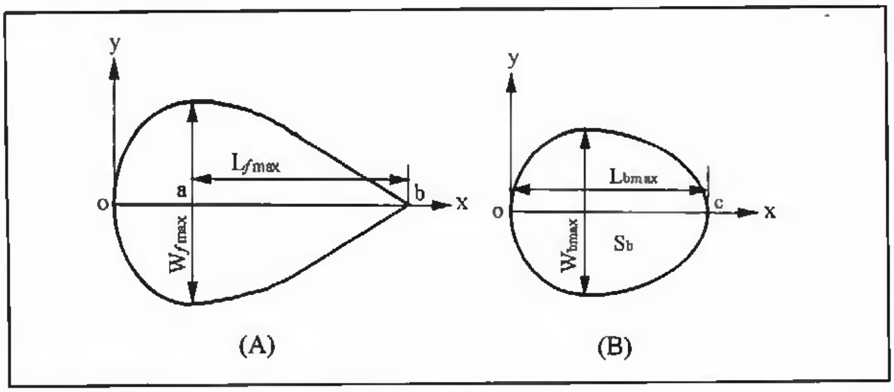

Fig. 5 — The definition of feature size parameters of a fully penetrated weld pool. A — Topside; B — backside.

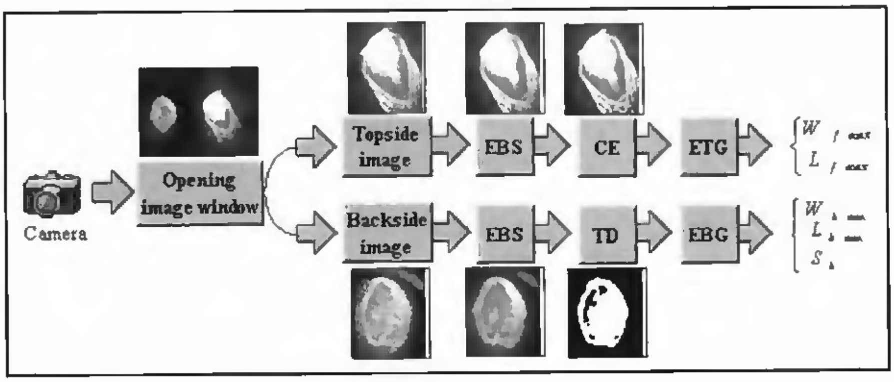

Fig. 6 — Signal flow chart of processing images of the weld pool.

M_3 and M_4 are reflectors, the centers of which are O_1, O_2, O_3 and O_4. O_1A, O_2B, O_3C and O_4D represent the normal line of the reflectors, respectively, denoted as the angles with each single axis in the coordinate system.

Along with a video recorder and monitor system, the visual sensing system consisted of the following parts.

<u>Light Path of Double-Sided Imaging Simultaneously in a Frame</u>

The light path was composed of topside and backside imaging light paths. Figure 2B shows the photograph of the double-sided visual sensing system, and Fig. 2A shows its schematic diagram. The light from the weld pool reached the reflector O_1 at a 45-deg angle with the X axis, and is reflected to pass the composite filter, then reflected by O_2, and finally focused on the target of the CCD camera. The backside light path is shown in the downside of Fig. 2A. The light path system was mounted behind the weld pool to avoid the pollution caused from spatter, fume and smoke.

The composite filter system included topside and backside light paths. The topside image of the weld pool was formed by the illumination from arc emission in the spectral window of 600–700 nm. The topside light path consisted of a neutral density filter (2 mm depth, and the attenuation ratio of the lens was 1%) and a narrow band filter. (The center band was 661 nm, half-width 10 nm and peak attenuation ratio of the lens, 28.8%.) The backside image was formed by the radiance of the backside hot metal. Two neutral density filters were used in the backside light path with lens attenuation ratios of 10 and 50%. Both the topside and backside images concentrated on the same target of the CCD camera through the above double-sided visual sensing light path system.

<u>CCD Imaging System Transferring the Optical Signal to Video Signal</u>

The CCD imaging system included a CCD camera, optical lens and frame grabber. The focal distance of the lens was 50 mm. The sensitivity of the camera was 0.4 Lux, its area of target 5.24 x 6.4 mm, and the shutter was set at 1/1000 s.

Initial Experiment

Bead-on-plate experiments were conducted on low-carbon steel during pulsed GTAW using the double-sided visual sensing system, and the experiment conditions are tabulated in Table 1. Peak current was set at 120 A and travel speed was 2.5 mm/s.

A complete weld pool image in a frame is shown in Fig. 3, in which the left is the backside image and the right is the topside image. The image contrast is high. Nozzle, arc center, topside molten portion and topside solidified portion can be clearly seen in the topside image. The bright arc around the weld pool was effectively eliminated, and the shape of the tungsten tip emerged from the background. The backside weld pool image is also distinguishable from the background.

Analysis of the Visual Sensing Principle

Arc light emission is complex. The intensity of spectral distribution of the arc light is shown in Fig. 4A (Ref. 33). It includes a continuous spectrum with low intensity and line spectrums with high intensity (metal line, Ar atom and Ar ion spectrum).

The principle behind imaging the weld pool is to illuminate the weld pool with the continuous spectrum of the arc light emission. This is because the radiation flux of the metal-line spectrum is much weaker than that of the continuous

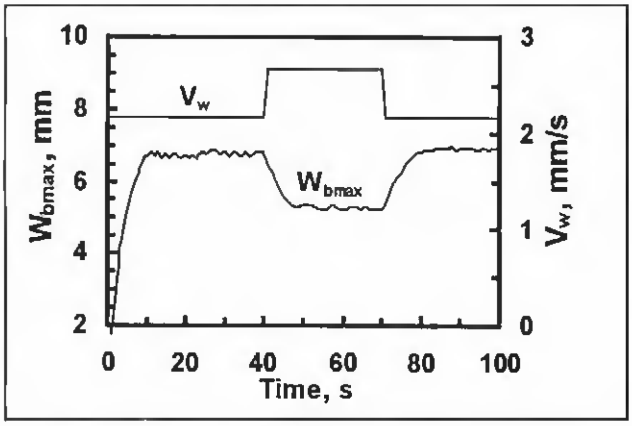

Fig. 7 — Transient response of backside width with travel speed.

arc spectrum. Figure 4B shows the arc light radiation flux of the whole spectrum through the narrow band filter.

In the range of 600–700 nm, there is mainly a continuous spectrum, with a few kinds of line spectrum, and the radiation flux is low and flat. So the spectral window 600–700 nm is suitable for lighting the weld pool.

Image Processing for the Weld Pool

For controlling the backside width, the correlation between topside maximum width and backside width is often adopted (Ref. 25). Experiments have shown the length of the topside weld pool changes more distinctly than the topside width with the variation of the heat-sinking condition. Also, the shape of the front part of the weld pool always keeps semicircle with the half-maximum-width as the radius, but the shape of the rear part of the weld pool changes significantly.

Thus, in this study, the topside geometry was specified by the maximum width W_{fmax}, and the maximum half-length L_{fmax} — Fig. 5A. The backside geometry parameters included the maximum width W_{bmax}, the length L_{bmax} and the area S_b — Fig. 5B.

According to the different characteristics of the topside and backside images, different image processing algorithms were developed. The flowchart of processing is shown in Fig. 6. In the figure, EBS is the exponential base-smoothing algorithm (Ref. 34); CE is the contrast-enhancement algorithm (Refs. 35–37); TD is the image-threshold algorithm of the backside weld pool; and ETG and EBG are the algorithm for determining topside geometry and backside geometry, respectively.

In topside image processing, after EBS and CE, the contrast between the edge of the weld pool and the background was improved. The welding direction was denoted as *fkw* and the vertical direction as *fkv*. The distribution of grayness along with *fkv* was like a mountain, which provided a feasible method for edge detection. The ETG algorithm included the following steps: finding the center, obtaining the gray value along with *fkv*, judging the edges, calculating the width, achieving the maximum width from comparison and deriving the maximum half-length.

In the backside image processing, the gray histogram of the filtered image with EBS showed the double-hump-shape prominently; therefore, the thresholding algorithm was suitable for image segment. The BTG algorithm included the following steps: finding the center, obtaining the gray value along with *fkv*, judging the edges, calculating the width, achieving the maximum width from comparison and deriving the maximum length and area.

On a PC-486 computer, the topside image processing algorithm lasted less than 50 ms, and the time of the backside algorithm was less than 30 ms. The pulse frequency of pulsed GTAW was 1 Hz and the time of base current was not less than 350 ms. So, the algorithms of the image processing were fast enough to fulfill the requirement of closed-loop control in real time.

Neural Network Model for the Dynamic Process

Weld pool geometry is a crucial factor in determining welding quality. In a previous study, the topside width of the weld pool was sensed and controlled (Ref. 25). To control the weld quality better, the correlation between the topside geometry and the backside width of the weld pool should be identified and modeled first.

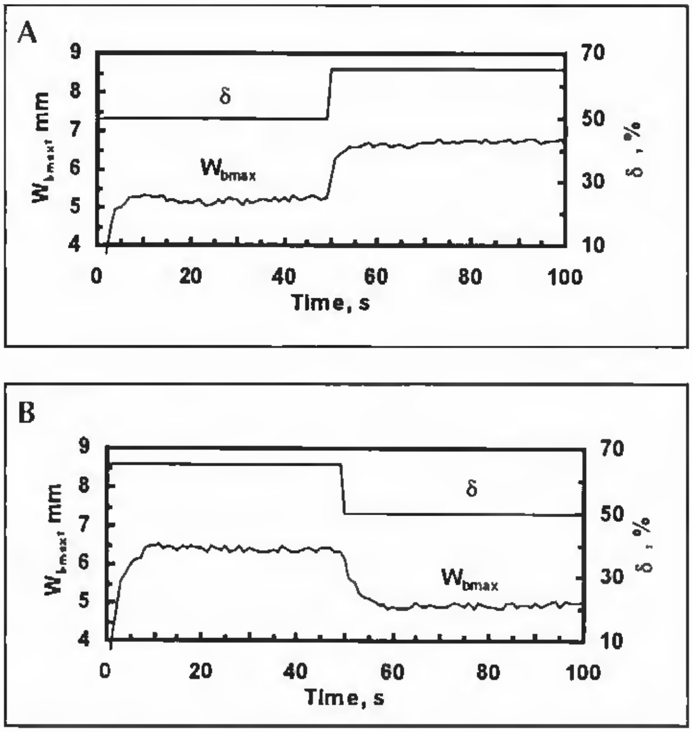

Fig. 8 — Transient response of backside width with pulse duty ratio. A — Positive step; B — negative step.

Conventional Identification of the Dynamic Process

To design a suitable control system, the dynamic characteristics of the welding process must be known, and the correlation between weld pool geometry and welding parameters must be established. In this study, step inputs were used to identify the transfer function. Generally, the welding process is considered as a first-order system with a given structure. The identification was thus simplified by estimating the model parameters. In pulsed GTAW, a skilled operator can make a near-perfect weld by regulating welding parameters such as pulse duty ratio and travel speed. Therefore, pulse duty ratio (δ) and travel speed (V_w) were adopted as the step inputs. Other conditions of the experiments were the same as in Table 1. Through experiment data, transient response of weld pool sizes with welding parameters (δ and V_w) were derived using the algorithm-of-area method developed with the Matlab program.

The designed step inputs and the step

response are shown in Figs. 7 and 8. The model parameters of the topside and backside geometry parameters were identified. Both the initiation and steady welding periods were considered. The feasibility of each model was verified by comparing the simulation results with the Matlab program and actual outputs.

The transfer functions of the backside maximum width-to-pulse duty ratio are exemplified as follows:

1) Initial period:

$$G_{W_{b\max}}(s)=\frac{W_{b\max}(s)}{\delta(s)}=\frac{0.101}{1.483s+1}e^{-\tau s}$$
$$\tau = 1s \tag{1}$$

2) Positive step in steady period:

$$G_{W_{b\max}}(s)=\frac{W_{b\max}(s)}{\delta(s)}=\frac{0.101}{2.068s+1} \tag{2}$$

3) Negative step in steady period:

$$G_{W_{b\max}}(s)=\frac{W_{b\max}(s)}{\delta(s)}=\frac{0.097}{2.785s+1} \tag{3}$$

The transfer functions of the backside maximum width to travel speed are exemplified as follows:

1) Positive step in steady period:

$$G_{W_{b\max}}(s)=\frac{W_{b\max}(s)}{V_w(s)}=\frac{-2.911}{3.328s+1} \tag{4}$$

2) Negative step in steady period:

$$G_{W_{b\max}}(s)=\frac{W_{b\max}(s)}{V_w(s)}=\frac{-3.242}{4.108s+1} \tag{5}$$

Other transfer functions were identified between other size parameters ($W_{f\max}$, $L_{f\max}$, $L_{b\max}$ and S_b) to pulse duty ratio and travel speed. From the identification results, the characteristics of the welding process were derived as follows:

- The three backside parameters respond to the variation in either δ or V_w at different speeds. $W_{b\max}$ reaches the steady state faster than $L_{b\max}$ and S_b, but slower than topside geometrical parameters.
- $W_{f\max}$ and $W_{b\max}$ respond to V_w more quickly than to δ, while $L_{f\max}$, $L_{b\max}$ and S_b are just opposite.
- During the steady-state period, the transfer functions of negative and positive step responses were different, which indicated nonlinearity of the process.
- The effects of δ and V_w on geometry were coupled with each other.

To investigate the complicated relationships between the weld penetration and welding parameters, neural networks were used because of their capability for modeling complicated nonlinear processes.

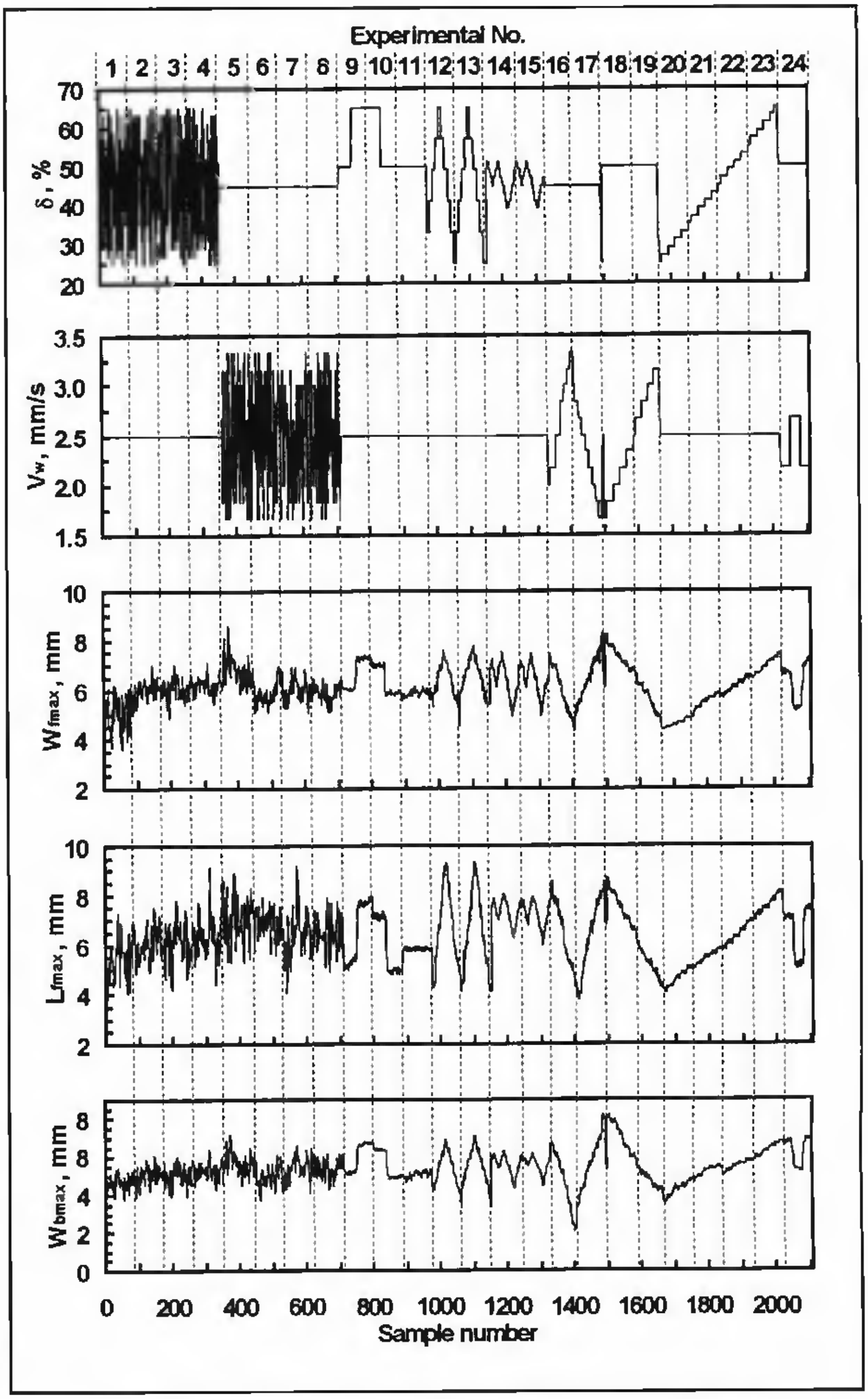

Fig. 9 — Experimental input signal and results considered in the experiments.

Experiments and Results for Neural Network Models

Variation in weld joint penetration could be influenced by welding parameters, experiment conditions and welding conditions. Welding parameters included pulse duty ratio, peak current, base current, arc voltage and welding speed, etc. Experiment conditions included the root opening or geometry of the groove, material, thickness, workpiece size, electrode tip angle and the rate of the shielding gas flow, etc. The welding conditions contained the heat-sinking condition. To form a valid method to monitor the weld joint penetration, the major parameters that may vary during welding were considered in the experiment design. Based on the analysis about the welding process, δ and V_w were selected as the input signal for exciting the characteristics of the welding process. Random and step signals were considered as the optimal input signals to the welding process. The weld pool size parameters were measured on-line during the experiments with the double-sided visual sensing system.

Twenty-four experiments were performed, and 2350 data pairs were obtained. The first ten results of each experiment were eliminated to avoid the effect of the transition process during the initial period, so 2110 samples were actually used. The results are shown in Fig. 9, arranged according to their serial number in the experiments.

Note the backside maximum width of weld pool varied widely, from 2 to 7.5 mm. The topside maximum width varied from 3.5 to 8.5 mm and the topside maximum half-length is from 3.5 to 9.5 mm. The variations of size parameters were caused by the different welding parameters or conditions.

Neural Network Model Architecture

An artificial neural network (ANN) provided a uniform model frame for almost all types of nonlinear functions. The actual inputs and outputs were taken as the training samples for the determination of the neurons' weight with the back propagation algorithm. In this study, a topside neural network model (TNNM), for describing the correlation between welding parameters and topside weld pool geometry, and a backside neural network model (BNNM), for predicting the backside width, were established.

Welding parameters, such as pulse duty ratio, peak current, base current, arc voltage and welding speed, were the major factors affecting heat input; the factors were also included in the model inputs. Because of the heat inertia of the welding process, size parameters responded to welding parameters with a time delay. Hence, the history information was included. For example, $V_w(t)$ meant the value of current pulse, $V_w(t-1)$ meant the value of last pulse and $V_w(t-2)$ meant the value of last before last pulse.

The principle of the ANN model is shown in Fig. 10. In the figure, TWP represents the topside welding process, TMS represents the topside measuring system, u is actual input variable of the system, y_t is actual output and y_{tm} is the output of TNNM. The error e_t was used for adjusting neuron weight in off-line training.

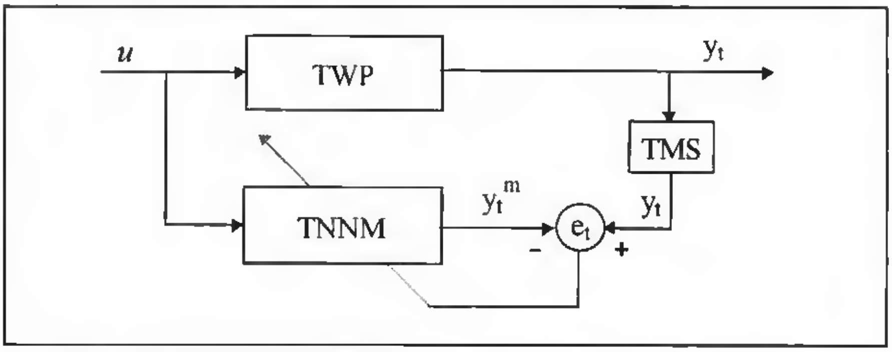

Fig. 10 — The principle of weld pool topside sizes modeling with a neural network.

The general architecture of the TNNM is shown in Fig. 11A.

For most applications, one hidden layer was sufficient. The number of elements in the hidden layer was selected based on the principle of minimum root-mean-square error (RMS). In TNNM, the number was selected from 12 to 25, and 14 BP networks were established. At last, by contrasting the root-mean-square error, it was determined the best number in the hidden layer was 23.

The training was performed using the

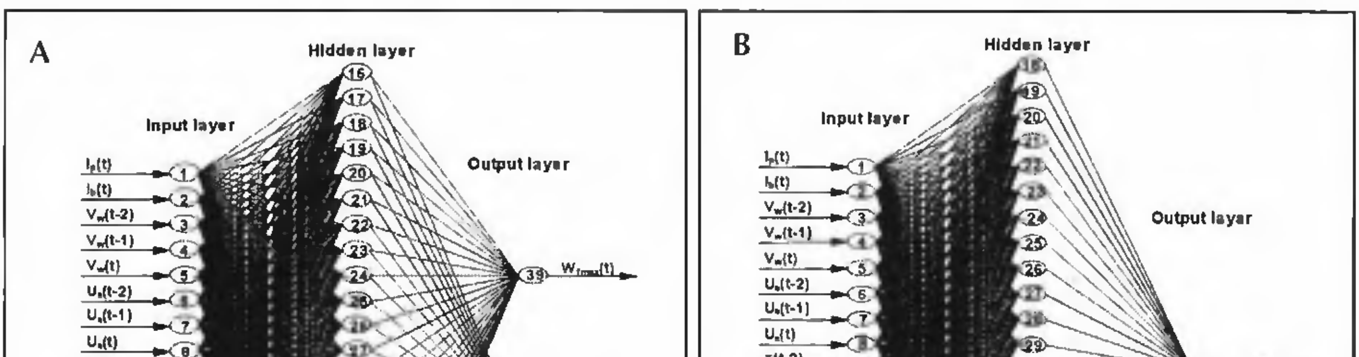

Fig. 11 — The architecture of a neural network dynamic model. A — TNNM; B — BNNM.

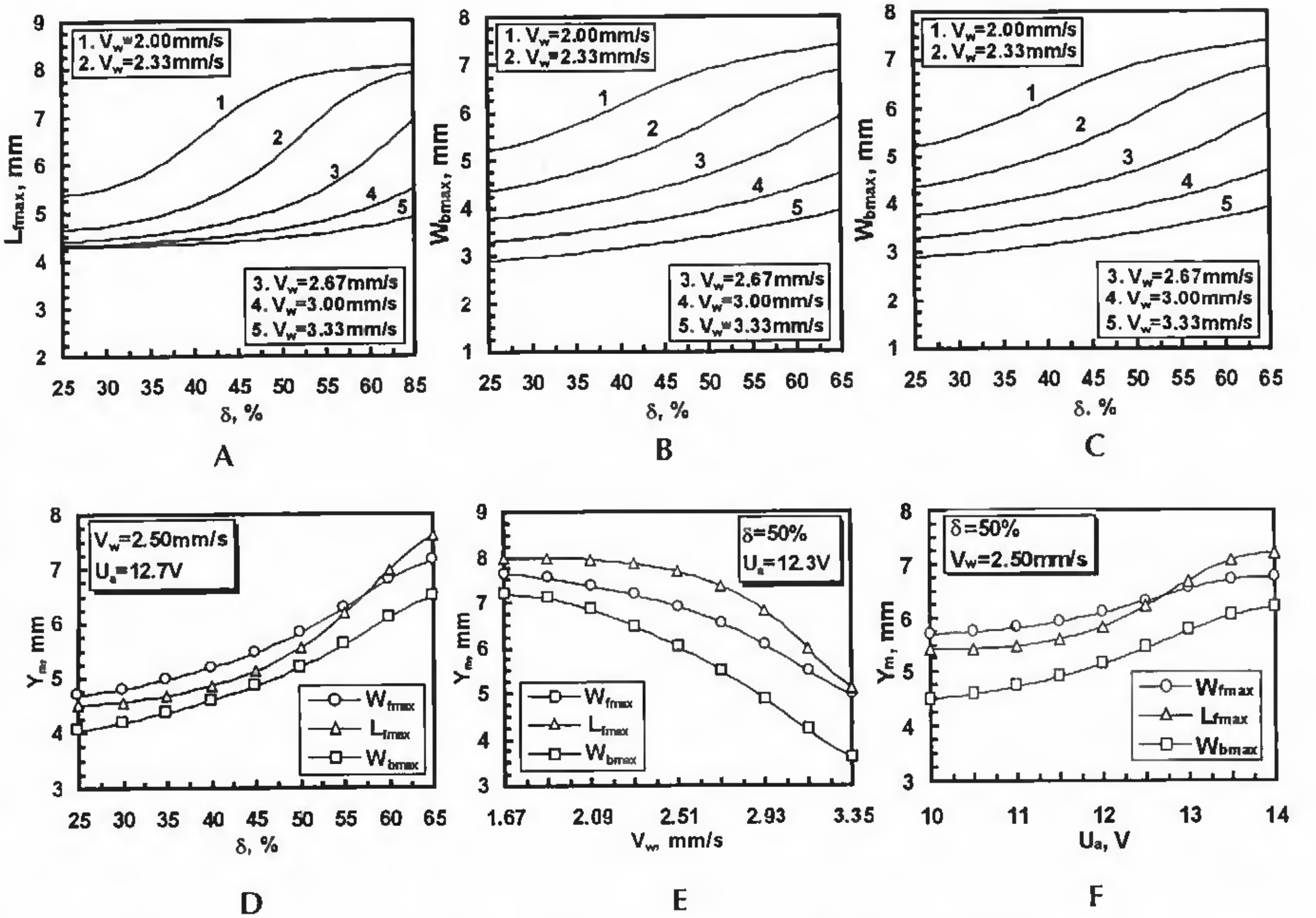

Fig. 12 — The dynamic output of TNNM and BNNM A — Topside maximum width with variation of welding speed; B — topside maximum half-length with variation of welding speed; C — backside maximum width with variation of welding speed; D — the relationship between weld pool size and pulse duty ratio; E — the relationship between weld pool size and welding speed; F — the relationship between weld pool size and arc voltage.

commercial neural network software, Professional Plus II. The sigmoid function was selected as the nonlinear function of the neuron. Delta-bar-delta (DBD) was selected as the learning algorithm, which could overcome the slow convergence associated with the conventional back-propagation algorithm. The learning coefficient and momentum ratio was automatically determined by the algorithm for each 5000 training cycle. The total training cycle was selected to be 20,000.

The RMS decreased to attain stable value with the increase of training numbers. The RMS of W_{fmax} was 3.97%, the RMS of L_{bmax} was 6.09% and the network was thought to be convergent and feasible. A total of 178 samples without training were used to verify the accuracy with good results: the RMS of W_{fmax} was 4.97% and the RMS of L_{bmax} was 3.42%.

BNNM was used for predicting the backside width. The architecture is shown in Fig. 11B. The inputs of the model included not only the input variables of TNNM but also the topside maximum width $W_{fmax}(t)$ and maximum half-length $L_{fmax}(t)$ of current pulse. The model principle was similar to TNNM. The number of elements in the hidden layer selected was 24. The RMS of W_{bmax} was 3.04%, and the network was thought to be convergent and feasible. A total of 178 samples without training were used to verify the accuracy with good results: the RMS of W_{bmax} was 4.01%.

Simulation and Discussion of Neural Network Models

The structure and parameters of TNNM and BNNM could be translated into C program, with which the output characteristic of the welding process could be simulated conveniently. Both static and dynamic output of TNNM and BNNM were analyzed with the simulation results. Figure 12 shows the outputs of TNNM and BNNM with the variations of δ and V_w during pulsed GTAW. The travel speed was 2.5 mm/s, the arc length 3.5 mm/s, the pulse peak current 120 A and the pulse base current 60 A. Other welding parameters and conditions were not changed.

Therefore, the following can be concluded:

1) At different V_w, size parameters such as W_{fmax}, L_{fmax} and W_{bmax} vary at different speeds with the increase of δ. When δ is small, the three size parameters increase slowly with the increase of δ, and even more slowly if V_w is large. When δ is large, the changes of the three parameters become complicated.

2) At constant V_w and U_a, the changes of W_{fmax}, L_{fmax} and W_{bmax} depend on δ differently. This indicates nonlinearity existing in the process.

3) At constant δ and U_a, W_{fmax}, L_{fmax} and W_{bmax} decrease with the increase of V_w.

4) At constant δ and V_w, W_{fmax}, L_{fmax} and W_{bmax} increase with the increase of arc voltage.

The above analysis shows welding parameters are coupled in determining the geometry parameters of the weld pool. W_{bmax} cannot be determined accurately by only W_{fmax}. The influence of L_{fmax} must be considered.

Contrast of Conventional and Intelligent Controllers

Under the variation of welding conditions, the present automatic welding machine could hardly produce the feasible control rules. Based on the complete analysis of the dynamic process, conventional and intelligent controls were designed and compared with each other, given the backside width as the control output and pulse duty ratio as the control variable.

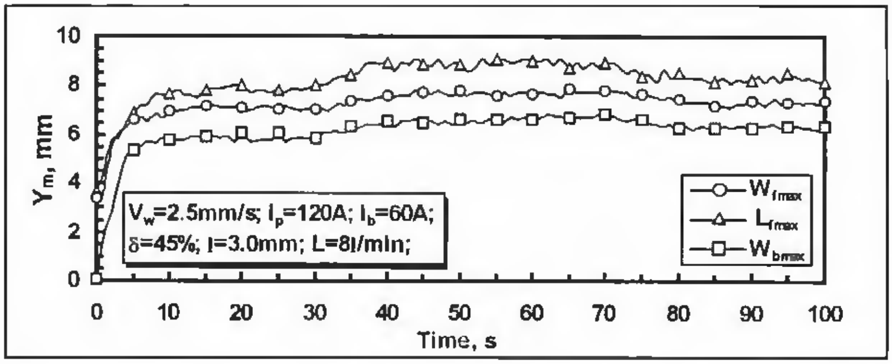

Fig. 13 — The weld pool sizes of the dumbbell-shaped workpiece under constant welding parameters.

Open-Loop Experiment

To verify the effectiveness of the developed control system, open-loop experiments were conducted for comparison. The specimens were mild steel plate 2 mm thick, and dumbbell shaped for imitating sudden changes in heat-sinking conditions during welding. From the test results shown in Fig. 13, the transition of weld pool size was distinguishable at 35 pulses and 70 pulses. From the photograph shown in Fig. 14, the weld sizes became larger when the size of the workpiece became narrower and the backside weld became poor.

PID Control

The PID control is the most widely used control algorithm. The increment algorithm was adopted because of the following characteristics: taking the increment variable as output, its calculation without sum and little impulse with hindrance. The increment algorithm with a four-point difference was denoted as follows:

$$\Delta u(k) = q_0 e(k) + q_1 e(k-1) + q_2 e(k-2) + q_3 e(k-3) + q_4 e(k-4)$$

$$q_0 = K_p\,(1+T/2T_i+T_d/6T)$$
$$q_1 = K_p\,(-1+T/2T_i+T_d/3T)$$
$$q_2 = -K_p \cdot T_d/T$$
$$q_3 = K_p \cdot T_d/3T$$
$$q_4 = K_p \cdot T_d/6T \qquad (6)$$

where K_p is the proportional coefficient, T_i is the integral constant, T_d is the differential constant and T is the sampling cycle.

To complete different control effects with the given output value, the coefficients of the controller, such as K_p, T_i and T_d, were determined first. With the backside width at 5.0 mm and a method of finding optimum multivariables, the coefficients of the controller were set with $K_p = 24.45$, $T_i = 0.585$ and $T_d = 0.795$.

Fuzzy Control

Unlike the conventional control scheme, fuzzy logic control is based not on a mathematical or physical model but on skilled workers' experience. It is a suitable method for the complex system. Generally, fuzzy control design includes determining the structure of fuzzy control, designing control rules, establishing fuzzy correlation and calculating the defuzzier.

The inputs of fuzzy control were the error and error change and the output was the pulse duty ratio. The accurate set of error was defined as e = [–2 mm, 2 mm]. The set of error change was ce =[–1.5 mm, 1.5 mm] and the set of pulse duty ratio change cu =[–15%, 15%].

Fuzzy variable sets of error and error change were denoted as E and CE and its region was {–6, –5, –4, –3, –2, –1, 0, 1, 2, 3, 4, 5, 6}. The fuzzy variable set of pulse duty ratio change CU was {–7, –6, –5, –4, –3, –2, –1, 0, 1, 2, 3, 4, 5, 6, 7}. Then, the quantitized factors were K_e = 3.00, K_{ce} = 4.00 and K_u = 2.143.

The word sets of CU and CE were defined as {NB, NM, NS, O, PS, PM, PB} and E was {NB, NM, NS, NO, PO, PS, PM, PB}. A bell-shaped normal function was selected as the subordinate function. Control rules were selected with the general rules of hot forming, with a sum of up to 56 rules.

The control rules can be described as fuzzy correlation for obtaining the set of control variables u. The method of gravity center was selected as the defuzzier method.

Then, the fuzzy control reference table could be derived (Table 2). During actual welding, the sampled e and ce were multiplied with K_e and K_{ce} to derive the column and row value. The output value was attained by looking up the

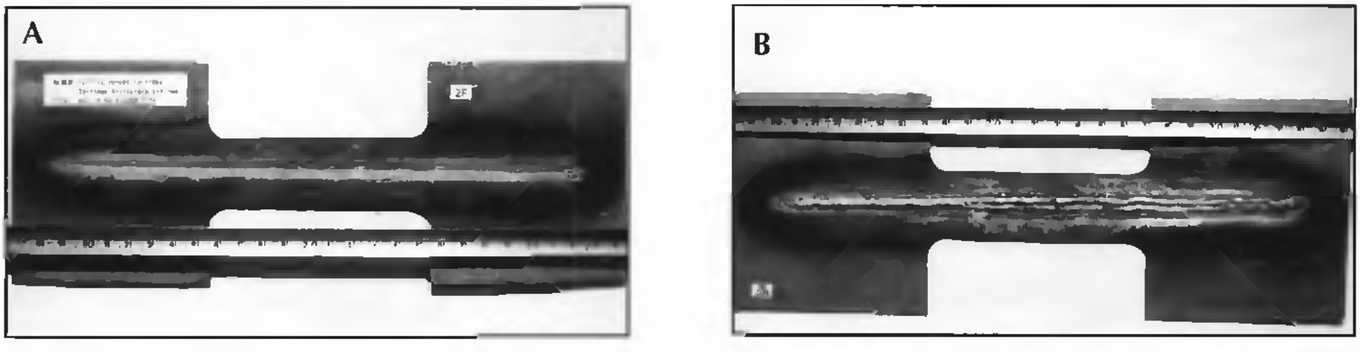

Fig. 14 — Photographs of dumbbell-shaped workpiece under constant conditions. A — Topside; B — backside.

Table 2 — The Reference Table for the Fuzzy Controller

CU\CE E	−6	−5	−4	−3	−2	−1	0	+1	+2	+3	+4	+5	+6
−6	7	6	7	6	7	6	6	5	3	2	1	0	0
−5	6	6	6	6	6	6	5	5	3	2	1	0	0
−4	7	6	7	6	7	6	5	4	3	2	1	0	0
−3	5	5	5	5	5	5	4	3	2	1	0	−1	−1
−2	4	4	4	4	4	4	3	2	1	0	0	−2	−2
−1	4	4	3	3	2	2	2	1	−1	−2	−3	−3	−3
−0	4	4	4	3	2	1	0	0	−1	−3	−3	−4	−4
+0	4	4	3	3	1	0	0	−1	−2	−3	−4	−4	−4
+1	3	3	3	2	1	−1	−2	−2	−2	−3	−3	−4	−4
+2	2	2	0	0	−1	−2	−3	−4	−4	−4	−4	−4	−4
+3	1	1	0	−1	−2	−3	−4	−5	−5	−5	−5	−5	−5
+4	0	0	−1	−2	−3	−4	−5	−6	−7	−6	−7	−6	−7
+5	0	0	−1	−2	−3	−5	−5	−6	−6	−6	−6	−6	−6
+6	0	0	−1	−2	−3	−5	−6	−6	−7	−6	−7	−6	−7

Table 3 — The Control Accuracy of Three Controllers

	10 ~ 30 pulses		31 ~ 70 pulses		71 ~ 100 pulses	
Time Errors Unit	Average error mm	Maximum error mm	Average error mm	Maximum error mm	Average error mm	Maximum error mm
PID control	0.14	0.32	0.21	0.40	0.17	0.36
Fuzzy control	0.13	0.38	0.25	0.51	0.12	0.42
PSD control	0.07	0.25	0.12	0.27	0.09	0.30

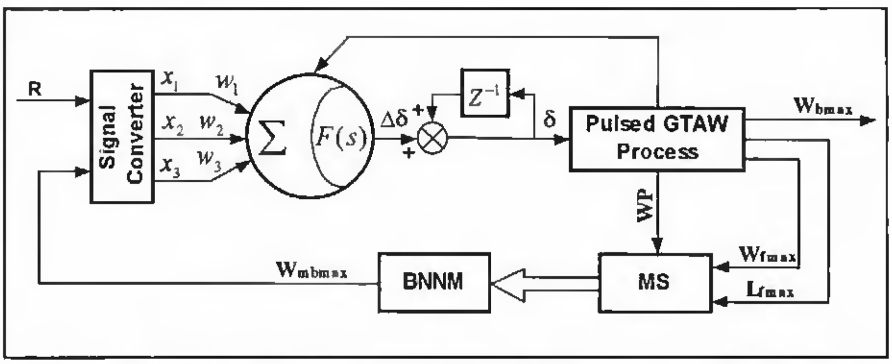

Fig. 15 — The schematic diagram of a single neuron self-learning PSD control system during pulsed GTAW.

value in the table, then multiplying it with a proportional factor K_{cu} to receive the actual variation of pulse duty ratio.

Neuron Self-Learning PSD Control

Aiming at the characteristics of changing structure and coefficients, a neuron self-learning PSD (proportional, sum and differential) control was proposed based on a single neuron. Only the desired output and the real output detected on-line were needed to form the neuron self-learning closed-loop control system, without on-line identification of the process coefficients. The weights of the neuron were corrected on-line with the improved BP algorithm and the error was minimized for optimizing the output of the control system.

The schematic of the neuron self-learning PSD control system is shown in Fig. 15. The output parameters of the welding process are size parameters, such as W_{fmax}, L_{fmax} and W_{bmax}; W_{bmax} is the controlled variable. MS is the measuring system for detecting topside size parameters (W_{fmax} and L_{fmax}) and welding parameters such as welding current, arc voltage, travel speed, etc.

These variables, combined with the values of the last two pulses, totaling 17 values, were as the input of BNNM. W_{mbmax} was the predicted backside with BNNM, inputted to the signal converter with the given backside width R. The output variables $X = \{X_1, X_2, X_3\}$ generated by the signal converter were inputted into the neuron self-learning PSD controller. The controller summed the variables X and determined $\Delta\delta$ with the nonlinear transfer function. At the same time, the input weights of the neuron were adjusted on-line with a BP algorithm by the error of backside width, to keep the control within the optimized state.

The input variables $X = \{X_1, X_2, X_3\}$ of the controller were error, error of first-order differential and error of second-order differential respectively, between the desired backside width and BNNM output, as follows:

$$
\begin{aligned}
x_1 &= \alpha_1 e(t) = \alpha_1 [R - W_{mbmax}(t)] \\
x_2 &= \alpha_2 \Delta e(t) = \alpha_2 [e(t) - e(t-1)] \\
x_3 &= \alpha_3 \Delta^2 e(t) = \alpha_3 [e(t) - 2e(t-1) + e(t-2)]
\end{aligned} \tag{7}
$$

where α_1, α_2 and α_3 are constant weights, selected as $\alpha_1 = 1.0$, $\alpha_2 = 0.3$ and $\alpha_3 = 0.1$.

Weight normalization is to avoid the saturation of weights during the learning process, as follows:

$$
w_i' = w_i \Big/ \sqrt{\sum_{i=1}^{3} w_i^2} \tag{8}
$$

The weight sum of the neuron's inputs is

$$
s = \sum_{i=1}^{3} w_i' \bullet x_i \tag{9}
$$

$F(s)$ is a nonlinear transfer function, selected as hyperbolic tangent function,

$$
\Delta\delta = F(s) = \gamma(1 - e^{-\xi s})/(1 + e^{-\xi s}) \tag{10}
$$

where γ and ξ are two constants. The saturated value of the control variable is determined by γ, and ξ determines the linear degree of the control variable. The larger the γ, the more possible it is to attain the desired value. The smaller the ξ, the wider the linear work region to restrain the fluctuation of the stable state. γ was selected as 300 and ξ as 0.135.

Object function was minimized by the following cost function:

$$E(w) = \frac{1}{2}\sum_{k}\left[R - W_{mb\max}(k)\right]^2 \tag{11}$$

The derived corrected formula of weight was as follows:

$$\Delta w_i = \eta\phi x_i$$
$$w_i(k+1) = w_i(k) + \Delta w_i, i = 1,2,3 \tag{12}$$

where $\eta = 1.0$ is the learning rate. ϕ is the equalized output error of neuron, resembling the actual output error.

$$\phi = [R - W_{mb\max}(k)] \cdot [1 - \Delta\delta(k)/\gamma] \cdot [1 + \Delta\delta(k)/\gamma] \tag{13}$$

Simulations of control performance were conducted with the developed neuron self-learning PSD controller. The desired outputs of the backside maximum width were set as 4.0, 4.5 and 5.0 mm.

Figure 16A shows the simulation results based on BNNM with R = 5.0 mm. The maximum overshoot was 2.81%, the regulating time 2 s, the steady-state error 0.04 mm and the pulse duty ratio stabilized at 42%.

Figure16C shows the simulation results with R = 4.5 mm. The maximum overshoot was 2.71%, the regulating time 2 s, the steady-state error 0.02 mm and the pulse duty ratio stabilized at 36%.

Figure16E shows the simulation results with R = 4.0 mm. The maximum overshoot was 2.25%, the regulating time 2 s, the steady-state error 0.01mm and pulse duty ratio stabilized at 27%.

Figures 16B, D and F show the weights. Similar simulations were conducted with the PID controller and fuzzy controller.

Results show the maximum overshoot of the neuron self-learning PSD is similar to the PID and fuzzy control, but the regulating time and steady-state error is smaller. Furthermore, the coefficients of the neuron can be adjusted on-line to make it capable of controlling the nonlinear process.

To test the feasibility of the neuron self-learning PSD control, experiments during pulsed GTAW were conducted. The control variable was the pulse duty ratio and its minimum regulating unit was 1%.

Figure 17 shows the neuron self-learning PSD control effect with R = 5.0 mm.

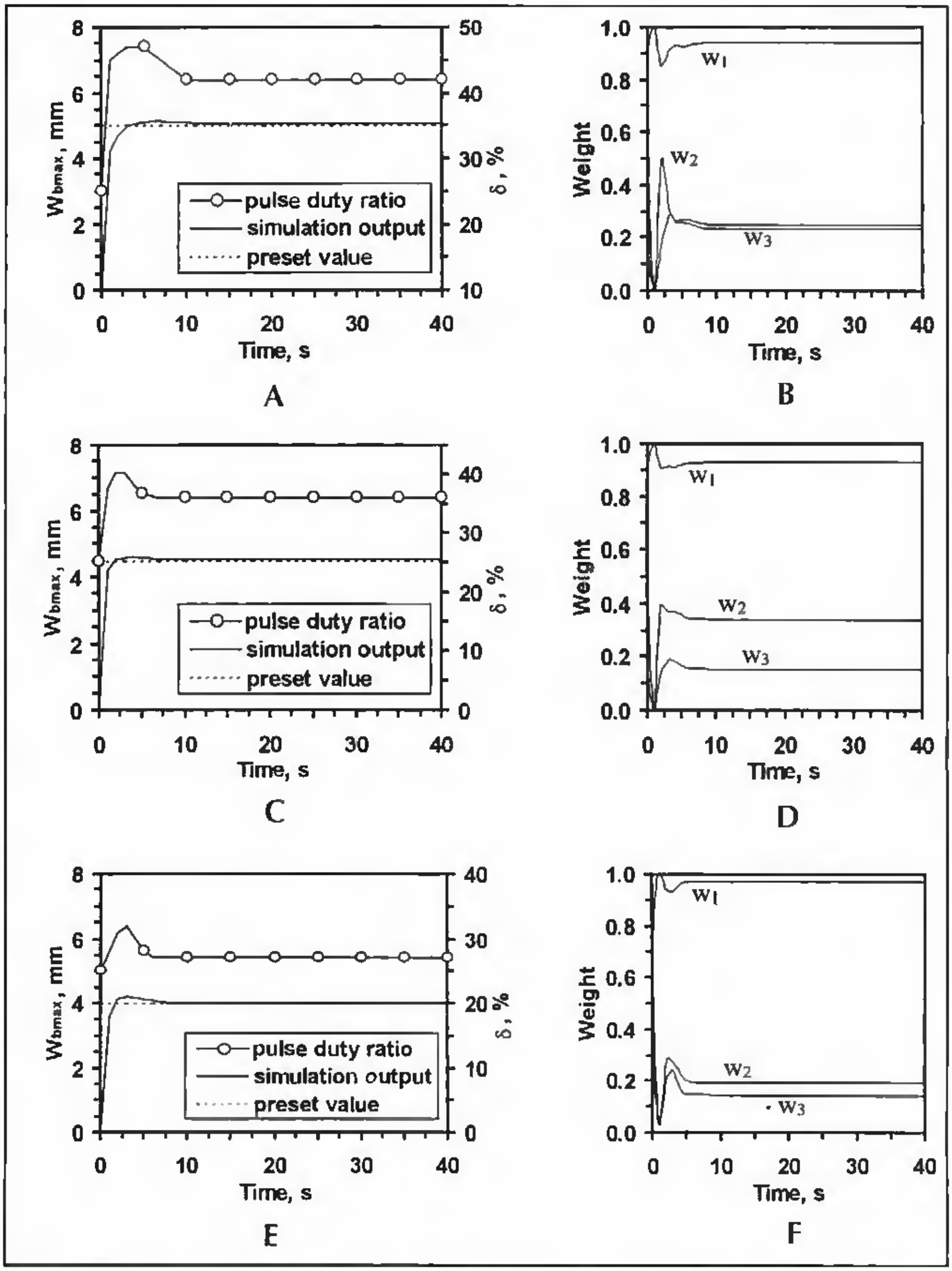

Fig. 16 — The simulation curve of the neuron self-learning PSD controller. A — W_{bmax} = 5.0 mm; B — the weight of W_{bmax} =5.0 mm; C — W_{bmax}=4.5 mm; D — the weight of W_{bmax} = 4.5 mm; E — W_{bmax} = 4.0 mm; F — the weight of W_{bmax} = 4.0 mm.

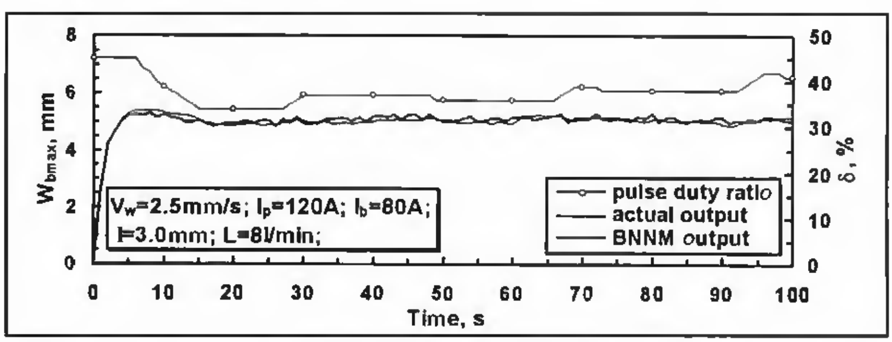

Fig. 17 — The neuron self-learning PSD closed-loop control curves of the dumbbell-shaped workpiece during pulsed GTAW.

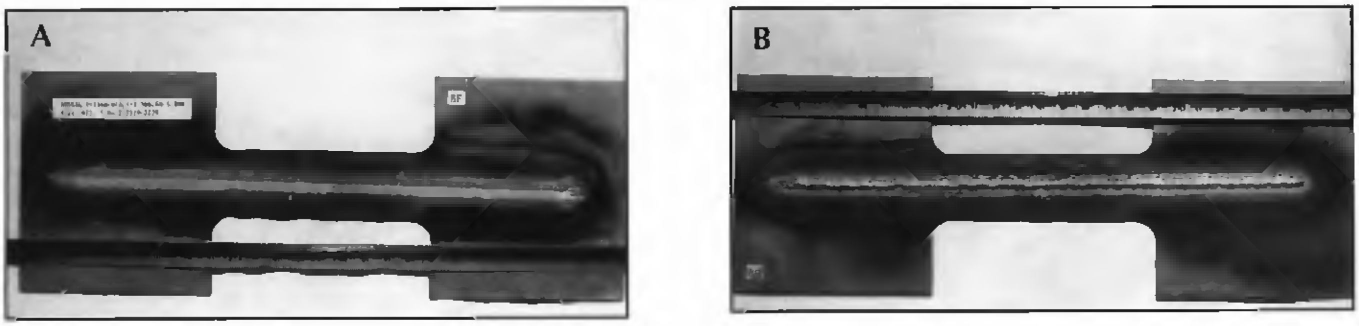

Fig. 18 — Photographs of dumbbell-shaped workpiece with neuron, self-learning PSD control. A — Topside; B — backside.

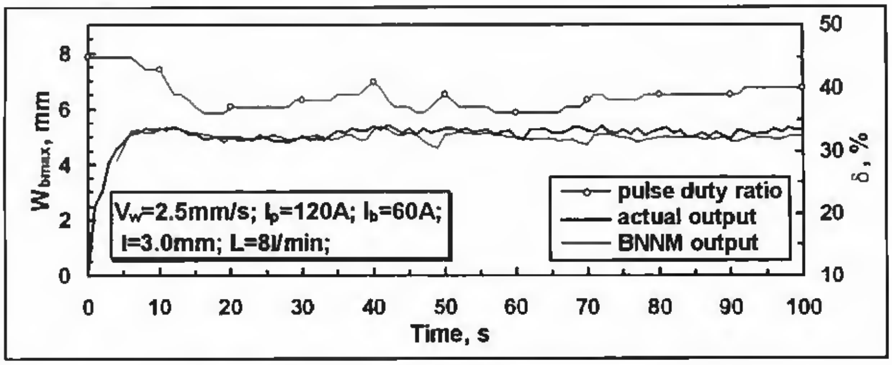

Fig. 19 — The PID closed-loop control curves.

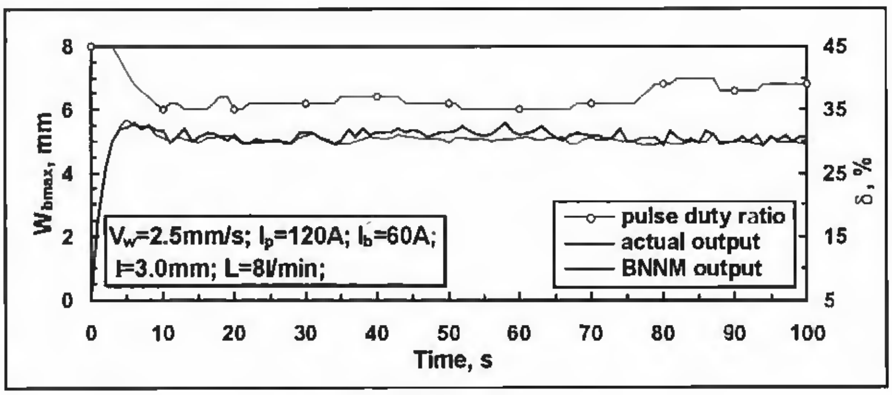

Fig. 20 — The fuzzy closed-loop control curves.

The control variable decreased with the heat-sinking conditions turning poor and increased with the condition reversing. The difference between BNNM output and set value R caused the variation of pulse duty ratio to keep the backside width maintained at 5.0 mm. The statistic results verified the feasibility of BNNM and neuron self-learning PSD control. The maximum error of BNNM output and test data was 0.26 mm. Test data were compared with the set value, the maximum error was 0.30 mm, the average error 0.10 mm and the root-mean-square deviation was 0.08 mm. The control results also verified the consistence with the simulation results. The perfect results of topside and backside photographs are shown in Fig. 18.

Discussion — Controls

Welding experiments with a conventional PID controller and fuzzy controller were conducted on a dumbbell-shaped specimen during bead-on-plate pulsed GTAW. The control curves are shown in Figs. 19 and 20. The statistic results of the three controllers are tabulated in Table 3. The initial ten pulses were omitted because the ignition period was not considered.

Results showed the accuracy of the PID and the fuzzy control are similar, with the maximum error less than 0.5 mm. The effect of the neuron self-learning PSD control was better, with the maximum error less than 0.3 mm. The errors of the middle period (31–70 pulses) were larger than that of both the start period (10–30 pulses) and the end period (71–100 pulses). This indicated the welding process becomes more complicated as the heat-sinking conditions turn worse.

The controllers designed were successfully implemented for pulse GTAW process control, but each PID control coefficient was limited to each desired backside width. Fuzzy control simulated the worker's experience, but did not possess the adaptive regulation with varied conditions. The neuron self-learning PSD control, however, attained a perfect control effect with different set values and conditions, and was suitable for the varied structure and coefficients of the welding process.

Conclusions

1) A new visual sensing system of imaging the topside and backside of the weld pool simultaneously in the same frame was established. The principle of obtaining a clear image of the weld pool with arc light illumination was analyzed.

2) A real-time algorithm of image processing was developed to acquire topside and backside sizes of the weld pool.

3) The dynamic characteristics of arc welding were investigated with positive and negative step responses. Furthermore, a more accurate model of pulsed GTAW was established by an artificial neural network.

4) Conventional and intelligent single-input and single-output control schemes were investigated. By careful comparison of the three controls, it was found that, under certain conditions, the PID controller and basic fuzzy controller can achieve good performance, and, in

most cases, the neuron self-learning PSD controller can achieve better, more robust control performance.

Intelligent methodology provided in this paper can be easily transplanted into other arc welding processes.

Acknowledgment

This work was supported by the National Natural Science Foundation of China, No. 59575057 and No. 59635160. The authors would like to thank the editor and anonymous referees for their careful review and constructive comments on the earlier versions of this article.

References

1. Duley, W. W., and Mao, Y. L. 1994. Effect of surface condition on acoustic emission during welding of aluminum with CO_2 laser radiation. *Journal of Physics D: Applied Physics* 27(7): 1379–1383.

2. Vilkas, E. P. 1966. Automation of the gas tungsten arc welding process. *Welding Journal* 45(5): 410-s to 416-s.

3. Suzuki, A., Hardt, D. E., and Valavani, L. 1991. Application of adaptive control theory to on-line GTA weld geometry regulation. *ASME Journal of Dynamics Systems, Measurement, and Control* 113(1): 93–103.

4. Bentley, A. E., and Marburger, S. J. 1992. Arc welding penetration control using quantitative feedback theory. *Welding Journal* 71(11): 397-s to 405-s.

5. Renwick, R. J., and Richardson, R. W. 1983. Experimental investigation of GTA weld pool oscillations. *Welding Journal* 62(2): 29-s to 35-s.

6. Zacksenhouse, M., and Hardt, D. E. 1983. Weld pool impedance identification for size measurement and control. *ASME Journal of Dynamics Systems, Measurement, and Control* 105(3): 179–184.

7. Wang, Q. L., Yang, C. L., and Geng, Z. 1993. Separately excited resonance phenomenon of the weld pool and its application. *Welding Journal* 72(9): 455-s to 462-s.

8. Xiao, Y. H., and Ouden, G. den 1993. Weld pool oscillation during GTA welding of mild steel. *Welding Journal* 72(8): 428-s to 434-s.

9. Xiao, Y. H., and Ouden, G. den. 1990. A study of GTA weld pool oscillation. *Welding Journal* 69(8): 289-s to 293-s.

10. Yoo, C. D., and Richardson, R. W. 1993. Experimental study on sensitivity and signal characteristics of weld pool oscillation. *Transactions of the Japan Welding Society* 24(2): 54–62.

11. Hardt, D. E., and Katz, J. W. 1984. Ultrasonic measurement of weld penetration. *Welding Journal* 63(9): 273-s to 281-s.

12. Lott, L. A. 1984. Ultrasonic detection of molten/solid interfaces in weld pools. *Materials Evaluation* 42(3): 337–341.

13. Carlson, N. M., and Johnson, J. A. 1988. Ultrasonic sensing of weld pool penetration. *Welding Journal* 67(11): 239-s to 246-s.

14. Carlson, N. M. 1992. Ultrasonic NDT methods for weld sensing. *Materials Evaluation* 50(11): 1338–1343.

15. Nagarajan, S., Chen, W. H., and Chin, B. A. 1989. Infrared sensing for adaptive arc welding. *Welding Journal* 68(11): 462-s to 466-s.

16. Chen, W., and Chin, B. A. 1990. Monitoring joint penetration using infrared sensing techniques. *Welding Journal* 69(4): 181-s to 185-s.

17. Beardsley, H., Zhang, Y. M., and Kovacevic, R. 1994. Infrared sensing of welding parameters for weld penetration control. *International Journal of Machine Tool and Manufacturing* 34(8): 1079–1090.

18. Kovacevic, R., Zhang, Y. M., and Li, L. 1996. Monitoring of weld joint penetration based on weld pool geometrical appearance. *Welding Journal* 75(10): 317-s to 329-s.

19. Kovacevic, R., Zhang, Y. M., and Ruan, S. 1995. Sensing and control of weld pool geometry for automated GTA welding. *ASME Journal of Engineering for Industry* 117(2): 210–222.

20. Kovacevic, R., and Zhang, Y. M. 1997. Real-time image processing for monitoring the free weld pool surface. *ASME Journal of Manufacturing Science and Engineering* 119(5): 161–169.

21. Kim, E. W., Allem, C., and Eagar, T. W. 1987. Visible light emissions during gas tungsten arc welding and its application to weld image improvement. *Welding Journal* 66(12): 369-s to 377-s.

22. Richardson, R. W., and Gutow, D. A. 1984. Coaxial arc weld pool viewing for process monitoring and control. *Welding Journal* 63(3): 43–50.

23. Pietrzak, K. A., and Packer, S. M. 1994. Vision-based weld pool width control. *ASME Journal of Engineering for Industry* 116: 86–92.

24. Brzakovic, D., and Khani, D. T. 1991. Weld pool edge detection for automated control of welding. *IEEE Transactions on Robotics and Automation* 7(3): 397–403.

25. Chen, S. B., Wu, L., Wang, Q. L., and Liu, Y. C. 1997. Self-learning fuzzy neural network and computer vision for control of pulsed GTAW. *Welding Journal* 76(5): 201-s to 209-s.

26. Pietrzak, K. A., and Packer, S. M. 1994. Vision-based weld pool width control. *ASME Journal of Engineering for Industry* 116(1): 86–92.

27. Song, J. B., and Hardt, D. E. 1994. Dynamic modeling and adaptive control of the gas metal arc welding process. *ASME Journal of Dynamics Systems, Measurement, and Control* 116(3): 405–413.

28. Andersen, K., and Cook, G. E. 1990. Artificial neural networks applied to arc welding process modeling and control. *IEEE Transaction Industry Application* 26(9): 824–830.

29. Lim, T. G., and Cho, H. S. 1993. Estimation of weld pool sizes in GMA welding process using neural networks. *Journal of Systems and Control Engineering* 207(1): 15–26.

30. Andersen, K., and Cook, G. E. 1992. Gas tungsten arc welding process control using artificial neural networks. Proceedings of the 3rd International Conference on Trends in Welding Research, Gatlinburg, Tenn., pp.135–142.

31. Kovacevic, R., and Zhang, Y. M. 1998. Neurofuzzy model-based weld fusion state estimation. *IEEE Control Systems* 17(2): 30–42.

32. Chen, S. B., Wu, L., and Wang, Q. L. 1997. Self-learning fuzzy neural networks for control of uncertain systems with time delay. *IEEE Transactions on System, Man, and Cybernetics-Part B: Cybernetics* 27(2):142–148.

33. Li., P. J. 1997. An applied basic research for arc light sensing in arc welding process. Ph.D. dissertation, Harbin Institute of Technology, Harbin, P. R. China.

34. Canny. 1986. A computational approach to edge detection. *IEEE Trans. on Image Processing* 28(2): 679–698.

35. Gordon, R., and Rangayan, R. M. Feature enhancement of film mammograms using fixed and adaptive neighborhood. *Appl. Opt.* 23(5): 560–564.

36. Dhawan, A. P., Buelloni, G., and Gordon, R. 1986. Enhancement of mammograms feature by optimal adaptive neighborhood image processing. *IEEE Trans. on Med. Imaging* 5(8): 8–15.

37. Beghdadi, A., and Negrate, A. L. 1986. Contrast enhancement technique based on local detection of edges. *Computer Vision Graphics Image Process* 46(9): 162–174.